

Halide-induced Step Faceting and Dissolution Energetics from Atomistic Machine Learned Potentials on Cu(100)

Mitchell C. Groenenboom,* Thomas P. Moffat, and Kathleen A. Schwarz

Material Measurement Laboratory

National Institute of Standards and Technology

Gaithersburg, MD 20899-8520 USA

E-mail: mitch.groenenboom@gmail.com

Abstract

Adsorbates impact the surface stability and reactivity of metallic electrodes, affecting the corrosion, dissolution, and deposition behavior. Here, we use density functional theory (DFT) and DFT-based Behler-Parrinello neural networks (BPNN) to investigate the geometries, surface formation energies, and atom removal energies of stepped and kinked surfaces vicinal to Cu(100) with a $c(2 \times 2)$ Cl adlayer. DFT calculations indicate that the stable structures for the adsorbate-free vicinal surfaces favor steps with $\langle 110 \rangle$ orientation, while the addition of the $c(2 \times 2)$ Cl adlayer leads to $\langle 100 \rangle$ step facets, in agreement with scanning tunneling microscopy (STM) observations. The BPNN calculations produce energies in good agreement with DFT results (root mean square error of 1.3 meV/atom for a randomly chosen set of structures excluded from the training set). We draw three conclusions from the BPNN calculations. First, Cl on the upper $\langle 100 \rangle$ step edges occupies the three fold hollow sites (as opposed to the four-fold sites on the terraces), congruent with deviations of the STM height profile for the adsorbate at the upper step edge. Second, disruptions in the continuity of the halide overlayer at the steps result in significant long-range step-step interactions. Third, anisotropic metal dissolution and deposition energetics arise from phase shifts of the $c(2 \times 2)$ adlayer at orthogonal $\langle 100 \rangle$ steps. This DFT-BPNN approach offers an effective strategy for tackling large-scale surface structure challenges with atomic-level accuracy.

Introduction

Surface adsorbates alter the composition, surface structure, and reactivity of electrodes. In deposition and dissolution reactions, adsorbates can act as intermediates, site blocking spectators, and/or structure-altering mediators of reactivity. Adsorbate guided dissolution can be applied to etch highly anisotropic structures,¹ but similar reaction conditions can lead to undesired effects, such as localized corrosion.^{2,3} Likewise, adsorbates also impact additive processes such as nanoparticle synthesis⁴⁻⁶ and the fabrication of multiscale microelectronic

interconnects.⁷

Understanding the energetics and geometry of adsorbate binding is central to determining surface evolution at electrode surfaces. Anionic adsorbates that form $c(2 \times 2)$ adlattices on (100) fcc metals represent useful benchmark systems in both electrochemical and ultra-high vacuum environments. These adsorbates induce surface reconstructions and step faceting, influencing kink formation and step flow during dissolution and deposition. Adsorbate-induced step faceting has been reported for Cl^- and Br^- adsorption on $\text{Cu}(100)$,⁸⁻¹⁵ I^- on $\text{Ag}(100)$ ¹⁶ and $\text{Pd}(100)$,¹⁷ and S^{2-} on $\text{Ni}(100)$.¹⁸ Monolayer steps can take two different forms, where the anion adlayer is either in- or out-of-phase between adjacent terraces. As shown later, geometrical constraints require that in-phase and out-of-phase structures alternate across orthogonal $\langle 100 \rangle$ oriented monolayer steps. The energetic difference between the two different step geometries gives rise to anisotropic mesoscale structures that are most evident during dissolution at small overpotentials.^{10,12,15}

While the phenomena associated with adsorbate-induced structural reconstruction and adsorbate-templated dissolution and deposition have been experimentally observed, the underlying energetic relationships have not been fully elucidated. First-principles methods such as density functional theory (DFT) can provide the accuracy necessary to distinguish between different adsorbate configurations but these methods are too computationally expensive to perform for the long length-scales required. Machine learned potentials show great promise for recreating and spatially extending DFT potential energy surfaces, and their relatively low computational cost facilitates calculations on systems that contain significantly more atoms than could be modeled with DFT.^{19,20}

Behler-Parrinello neural networks (BPNNs) are one particular type of atomistic machine learned potential that utilize standard artificial neural networks to calculate the atomic energies and forces of a given structure as a function of a mathematical representation of every atom's local environment.

BPNNs have been extensively developed over the past decade, and recent work has in-

creased their computational efficiency and has made modeling of large systems with many atom types possible.²¹ A number of codes are freely available for these calculations (i.e. AMP,²² the n2p2 C++ library,²³ Prophet,²⁴ and the Atomic Energy Network^{25,26}). Previous studies have used BPNNs to model the dynamics of water clusters,²³ sample catalyst configurations on a supported surface, simulate the structure of water on Cu²⁷ and ZnO^{28,29} surfaces, and predict the high temperature phase transformation of Cu₂S.³⁰ In summary, the flexibility of these potentials, their ability to reproduce DFT energetics, and their computational efficiency compared against DFT make BPNN potentials a promising candidate for studying the the adsorption of halide adlattices on extended surface structures.

Here we examine adsorbate-induced step faceting in the Cu(100)-c(2x2)Cl model system with DFT and BPNN calculations. We first identify the lowest-energy step edge structures and calculated their formation energies as a function of electrochemical potential from DFT calculations. After demonstrating that our BPNN could reproduce the results of our DFT calculations, we use our BPNN to study the energetics of larger step and island structures on Cu(100) surfaces. Although DFT calculations can provide similar insights in principle, many of the structures in this work contain more than 3000 atoms and are larger than can be studied with standard software for DFT calculations. We compare the height profiles of our BPNN predicted structures with those from electrochemical scanning tunneling microscopy (STM) data. Using BPNN calculations, we demonstrate that long-range interactions between steps can be induced by Cl adlattice disruptions. Lastly, we calculate Cu dissolution energies for individual atoms along steps and islands with our BPNN potential. Our calculations assume that ion-transfer reactions remove Cu atoms from the surface, but the reverse processes may also play a role in electrocrystallization reactions.

Methods

Density Functional Theory

All DFT calculations in this work were performed with Quantum Espresso.^{31,32} All calculations utilized Fermi-Dirac smearing with Gaussian spreading of 0.01 Ry (≈ 0.14 eV) and the revised Perdew-Burke-Ernzerhof (revPBE)³³ generalized-gradient-approximation DFT exchange correlation functional. These calculations utilized the Cl.pbe-n-kjpaw_psl.1.0.0.UPF and Cu.pbe-dn-kjpaw_psl.1.0.0.UPF pseudopotentials from <http://www.quantum-espresso.org>. An 8x8x8 k-point grid and a kinetic energy cutoff of 100 Ry gave well-converged energies for bulk FCC Cu with a geometry optimized lattice parameter = 0.366 nm (experiment = 0.3615 nm). All slab models were periodic in the x- and y-direction, composed of 4 to 5 layers, and separated by 2 nm of vacuum space in the z-direction. Slab and bulk calculations had identical kinetic energy cutoffs, and equivalent k-point grids in the x and y directions of the slab, that were inversely proportional to the number of primitive Cu unit cells used to compose the slab in those directions. A single k-point for the slab was used in the z direction. We did not include dispersion effects because the strong chemisorption interactions between Cl atoms and the copper surface dominate the adsorption energetics

We use the computational hydrogen electrode with no electrolyte effects to calculate the potential dependence of chloride adsorption. The double layer structure of the metal-adsorbate-electrolyte interface, and the Cu(100) surface with a Cl c(2x2) adlayer in particular, is an area of active debate.³⁴⁻³⁶ However, there is no established best procedure for capturing these electrolyte effects with computational models. As a first approximation, we choose to omit solvation and electrification effects. This allows us to consider the longer length-scales that are made accessible by BPNNs, which have not yet been fully developed and tested for charged, solvated interfaces.³⁷ The similarity between the step faceting of c(2x2)Cl-Cu(100) in vacuum¹² and the electrochemical environment⁹⁻¹¹ suggests that this approximation is reasonable.

Note: Certain commercial materials are identified in this paper to foster understanding. Such identification does not imply recommendation or endorsement by the National Institute of Standards and Technology, nor does it imply that the materials or equipment identified is necessarily the best available for the purpose.

Training Behler-Parrinello Neural Networks

To train a Behler-Parrinello neural network (BPNN) capable of modeling both the c(2x2) chloride adlattice and the underlying Cu surface, we generated a training set that contained the structures, DFT energies, and DFT atomic forces of 880 unique Cu surfaces with and without a c(2x2) Cl adlayer. These structures consisted of Cu(100) terraces, Cu(100) terraces that contained steps aligned in the [100] or [110] directions, Cu(111) terraces, and Cu(111) terraces with steps aligned in the [011] and [112] directions. Each structure was fully optimized with and without Cl adsorbed on the surface, in a fully occupied c(2x2) Cl adlattice for Cu(100) or a fully occupied $(\sqrt{3}\times\sqrt{3})R30^\circ$ for Cu(111).

We created all step structures by starting with a flat Cu(100) surface and removing Cu atoms from the top layer to produce steps in the previously listed directions. The training set also contains steps on the Cu(111) surface that were created using this approach. To maintain periodicity, these models for Cu(111) included two steps in a given DFT or BPNN calculation. This approach produced asymmetrical steps on the Cu(111) surface. This work primarily investigates the Cu(100)-c(2x2)Cl surfaces, and the asymmetry in our Cu(111) step structures does not effect our calculations on these surfaces.

The initial structure, final structure, and three intermediate structures from each geometry relaxation were included in the training set (140 total structures). To supplement these data points, we used the rattle function from the atomic simulation environment³⁸ to perturb fully optimized slab structures. The rattle function displaced every atom in the slab by randomly selecting a displacement from a normal distribution with a set standard deviation. We selected standard deviations of 0.1, 0.18, and 0.25 Å and generated 20 randomized

structures for every standard deviation. The energies and atomic forces of every new structure (560 total structures) were then calculated with DFT and included in the training set. Finally, we created 180 structures where only one Cl atom was displaced in the +x, -x, +y, -y, +x +y, and -x -y directions by 0.25, 0.50, 0.75, 1.0, and 1.25 Å. These displacements were performed on the Cu(100) terraces that contained steps aligned in the [100] direction and Cu(100) terraces that contained steps aligned in the [110] direction for three different Cl coverages. All training set structures are provided in the supplemental information. The energies in the training set (E^{train}) were normalized according to Equation 1,

$$E^{train} = E_{slab}^{DFT} - mE_{Cu,bulk}^{DFT} - \frac{n}{2}E_{Cl_2}^{DFT} \quad (1)$$

where m is the number of Cu atoms in the slab, $E_{Cu,bulk}^{DFT}$ is the DFT energy of a bulk Cu atom, n is the number of Cl atoms in the slab, and $E_{Cl_2}^{DFT}$ is the DFT energy of a gas phase Cl_2 molecule.

We used the n2p2 C++ library²³ and its LAMMPS³⁹ implementation to train and use atomistic BPNNs. We used 80% of our data set as a training set and 10% as a test set to prevent overfitting during the BPNN training. The remaining structures were withheld from the training procedure and used as a validation set. Our neural network consisted of an input layer and a single output neuron that were connected by two hidden layers that each contained 30 softplus activated nodes. The input layer consisted of 38 symmetry functions for Cu (24 weighted radial symmetry functions and 14 weighted angular symmetry functions) and 44 symmetry functions for Cl (8 radial symmetry functions for Cl-Cl interactions, 22 weighted radial symmetry functions, and 14 weighted angular symmetry functions). We selected these symmetry functions based on the scheme recommended by Gastegger et. al.²¹

Weighted atom centered symmetry functions (wACSFs) only require one set of radial and angular functions to describe the environment of each atom type. This is a significant improvement over previous implementations of atom centered symmetry functions (ACSFs)⁴⁰ that required unique sets of radial and angular functions for every combination of atom types

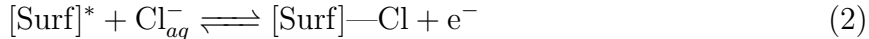
For example, ACSFs require three sets of radial functions for a Cu-Cl system (Cu-Cu, Cu-Cl, Cl-Cl pairs), while only two sets of wACSFs are needed (Cu-X and Cl-X where X is either Cu or Cl). wACSFs avoid cross terms for different atom types by using a general radial or angular function and modifying the value for each neighboring species with an internally parameterized weighting function. The number of required wACSFs scales linearly with the number of atom types, while the number of required ACSFs scales exponentially. Because of this, BPNNs trained with wACSFs generally require fewer computational resources than BPNNs trained with an analogous set of ACSFs when more than one atom type is present. Because the number of required wACSFs scales linearly with the number of atom types, our use of wACSFs allows us to easily expand our BPNN to include the presence of solvents or additional adsorbate species in future work. wACSFs have already been shown to be capable of simulating of systems with up to 12 atom types while maintaining chemical accuracy with respect to the DFT training data (<5 meV/atom error).²¹

We trained the BPNN with the multi-stream Kalman filter training method implemented in the n2p2 library along with the training parameters recommended by Singraber.³⁰ The BPNN was satisfactorily converged within 20 training epochs. The final BPNN had an $E_{train}^{rmse} = 2.3$ meV/atom, an $E_{test}^{rmse} = 1.3$ meV/atom, an $F_{train}^{rmse} = 45$ meV/Å, and an $F_{test}^{rmse} = 53$ meV/Å. These RMSE values suggest that the BPNN is not overfit to the training set. The BPNN accuracy with respect to our initial DFT calculations is shown in Figures S3, S4, and S5.

All reported BPNN structures were created by removing atoms from flat Cu(100) terraces with a c(2x2)Cl adlayer to produce the desired surface geometry. The structures were then fully relaxed at 0K using LAMMPS with our final BPNN potential (force convergence criteria of 0.01 eV/Å).

Step edge formation energies and adsorption potentials

Chloride (Cl_{aq}^-) oxidatively adsorbs to vacant adsorption sites on Cu surfaces ($[\text{Surf}]^*$) according to Equation 2.



We model chloride adsorption to Cu surfaces following the work of McCrum et al.⁴¹ The Gibbs free energy of chloride is challenging to calculate with DFT, but it can be related to that of gas phase chlorine with Eqs. 3 and 4.



$$\Delta G^{\text{redox}} = G_{\text{Cl}_{\text{aq}}^-} - \left(\frac{1}{2}G_{\text{Cl}_{2(g)}} - eU_{\text{NHE}}\right) \quad (4)$$

All potentials are referenced on the normal hydrogen electrode (NHE) scale unless otherwise stated. Equation 4 calculates the Gibbs free energy of the redox reaction shown in Equation 3 as a function of the applied electrode potential (U_{NHE}). $\Delta G^{\text{redox}} = 0$ when U_{NHE} is equal to the equilibrium potential of Equation 3 ($U_{\text{Cl}_2/\text{Cl}_{\text{aq}}^-}$), so Equation 4 can be rearranged to yield the energy of aqueous chloride ($G_{\text{Cl}_{\text{aq}}^-}$) in terms of the energy of Cl_2 ($G_{\text{Cl}_{2(g)}}$) and the $\text{Cl}_2/\text{Cl}_{\text{aq}}^-$ redox potential ($U_{\text{Cl}_2/\text{Cl}_{\text{aq}}^-}$):

$$G_{\text{Cl}_{\text{aq}}^-} = \frac{1}{2}G_{\text{Cl}_{2(g)}} - eU_{\text{Cl}_2/\text{Cl}_{\text{aq}}^-} \quad (5)$$

The Gibbs free energy of chlorine ($G_{\text{Cl}_{2(g)}}$) is equal to the calculated gas-phase energy per atom of chlorine plus an energy correction to account for changing the concentration from the calculation reference point (1 atm) to the approximate experimental concentration (10^{-6} atm). The potential correction ($\Delta G = -RT \ln(V^*/V^o)$) is a function of the reference molar volume (V^o), experimental molar volume (V^*), and temperature. Using the ideal gas

law to relate the molar volume of $\text{Cl}_{2(g)}$ to its partial pressure, we calculate $\Delta G = -0.357$ eV/ $\text{Cl}_{2(g)}$. The $\text{Cl}_{2(g)}/\text{Cl}_{\text{aq}}^-$ redox potential near the relevant experimental conditions (10^{-6} atm $\text{Cl}_{2(g)}$ and 10^{-3} mol/L Cl_{aq}^-) is equivalent to the standard value,⁴² so we use $U_{\text{Cl}_2/\text{Cl}_{\text{aq}}^-} = 1.36 V_{NHE}$ for all calculations.

We calculate the formation energies of step edges (λ_{step}) on the Cu(100) surface as a function of applied potential (U_{NHE}) at a fixed chloride concentration in solution with the following equation:

$$\lambda_{step} = (G_{[Surf]} - N_{Cu}G_{Cu} - N_{Cl}(\frac{1}{2}G_{\text{Cl}_{2(g)}} - eU_{\text{Cl}_2/\text{Cl}_{\text{aq}}^-}) - N_{Cl}eU_{NHE} - \gamma_{terrace}A_{[Surf]})/L_{step} \quad (6)$$

where $G_{[Surf]}$ is the energy of the optimized surface, G_{Cu} is the energy per atom of bulk Cu, and $[\frac{1}{2}G_{\text{Cl}_{2(g)}} - eU_{\text{Cl}_2/\text{Cl}_{\text{aq}}^-}]$ is the energy contribution of an aqueous chloride defined by equations 3, 4, and 5. N_{Cu} and N_{Cl} are the number of Cu atoms and Cl atoms in the slab. eU_{NHE} accounts for the energy of electrons produced when chloride oxidatively adsorbs to the surface. R is the gas constant, T is temperature, $A_{[Surf]}$ is the surface area of the slab, and L_{step} is the length of the step-edge in the slab.

Equation 6 is based on the step formation energy equation used by Yu and Scheffler to quantify the energy penalty for creating steps on Ag(100) surfaces.⁴³ We modified the equation to account for the presence of an adsorbate species using the computational electrode model described in equations 3, 4, and 5. Computational electrode models were first used to approximate the free energy of oxygen reduction reaction intermediates on metal and metal alloy surfaces by Nørskov, Anderson, and their respective coworkers.^{44,45} This approach has since been used to study a variety of electrochemical processes, such as metal dissolution potentials,⁴⁶ nucleation rates for electrodeposition,⁴⁷ and the adsorption of halides on metal surfaces.⁴¹

The gas-phase surface formation energy of a flat terrace ($\gamma_{terrace}$) can be calculated with

Equation 7,

$$\gamma_{terrace} = (G_{[Surf]} - N_{Cu}G_{Cu} - N_{Cl}(\frac{1}{2}G_{Cl_2(g)} - eU_{Cl_2/Cl_{aq}^-}) - N_{Cl}eU_{NHE})/A_{[Surf]} \quad (7)$$

and subtracted from the quantity in equation 6 to yield a step formation energy. In Equation 7, $G_{[Surf]}$ and $A_{[Surf]}$ represent the DFT energy and surface area of a Cu(100) surface without a step edge. We calculate the energetics of steps and Cu(100) terraces with fully occupied Cl adlayers. As a result, the step formation energy trends will be most accurate at higher potentials ($> 0 V_{NHE}$) where the Cl adlattice is fully occupied. We model these systems at full coverage for two reasons: 1) to minimize the contribution of configurational entropy and 2) the experimental STM measurements and Cu dissolution measurements were made at conditions where the adlayer was effectively fully occupied.

We assume that changes in the surface phonons between the flat terrace surface model and one that includes step edges will be negligible. Therefore, our calculations ignore entropy corrections and zero point energy contributions. G_{Cu} , $G_{Cl_2(g)}$, and G_{Surf} are solely the DFT or BPNN energies of a bulk Cu atom, a gas-phase chlorine molecule, and the optimized surface structures. Exact free energy computations are computationally expensive, so we rely on the previously mentioned free energy approximations to streamline our computational procedure.⁴⁴⁻⁴⁶

Heatmap Generation with Behler-Parrinello Neural Networks

Cu removal heatmaps were generated through a four step procedure. First, we created a 5 layer thick Cu(100) surface that was 73.16 x 73.16 Å (20 x 20 fcc Cu unit cells). The bottom layer was fixed to the DFT determined coordinates of bulk Cu in all subsequent calculations. A 33 x 33 Å square island composed of [100] oriented steps was placed on top of the Cu slab. One corner of the island was removed to produce a short step in the [110] direction. A c(2x2)

chlorine adlattice was placed on the surface such that no domain walls were present in the adlattice with a given terrace. Second, we used the BPNN to fully optimize the previously described structure and calculate its energy (G_{Slab}^{BPNN}). Third, we systematically removed individual Cu atoms from the island, and used the BPNN to fully optimize the resulting structure and calculate its energy ($G_{Slab-Cu}^{BPNN}$). Finally, we calculated the energy required to oxidatively remove each individual Cu atoms from the island ($[Slab] \rightleftharpoons [Slab-Cu] + Cu_{(aq)}^{2+} + 2e^-$) with Equation 8,

$$\Delta G_{CuRemoval}^{BPNN} = G_{slab-Cu}^{BPNN} - 2eU_{NHE} + G_{Cu^{2+}(aq)}^{BPNN} - G_{slab}^{BPNN} \quad (8)$$

We can relate the energy of $Cu_{(aq)}^{2+}$ ($G_{Cu^{2+}(aq)}^{BPNN}$) to that of a bulk copper atom ($G_{Cu(s)}^{BPNN}$) with the copper redox reaction ($Cu^{2+} + 2e^- \rightleftharpoons Cu_s$) and Equation 9.

$$\Delta G^{redox} = G_{Cu(s)}^{BPNN} - (G_{Cu^{2+}} - 2eU_{NHE}) \quad (9)$$

$\Delta G^{redox} = 0$ when U_{NHE} is equal to the redox potential of copper ($U_{Cu/Cu^{2+}}$), so $G_{Cu^{2+}} = G_{Cu(s)}^{BPNN} + 2eU_{Cu/Cu^{2+}}$. Within this modeling approximation, the removal energy of every Cu atom ($\Delta G_{CuRemoval}^{BPNN}$) will vary linearly with the difference between the applied potential (U_{NHE}) and the Cu/Cu²⁺ redox potential ($U_{Cu/Cu^{2+}}$). We use the standard Cu/Cu²⁺ redox potential, and calculate all Cu removal energetics for $U_{NHE} = U_{Cu/Cu^{2+}}$. The energy required to remove a Cu atom from the island depends on the local environment. The removal energies displayed in this article are only accurate for the shown island shape because modifying the island structure will change the reactivity of nearby Cu atoms. $G_{Cu(s)}^{BPNN}$, $G_{Slab-Cu}^{BPNN}$, and G_{Slab}^{BPNN} are equivalent to the BPNN energy of the optimized structure and do not include entropy corrections or zero point energy contributions.

STM Measurements

A Laue X-ray aligned Cu (100) crystal was electropolished in 85% vol phosphoric acid followed by extensive rinsing with 18 M Ω water. The specimen was then transferred to the electrochemical STM cell that was filled with deaerated 0.01 mol/L HClO₄ + 0.001 mol/L NaCl and maintained under an argon atmosphere. A Cu wire was used as a quasi-reference electrode with a Pt-Ir counter electrode. Imaging was performed in a constant current mode where the z-axis corresponds to the voltage applied to the z-piezo scanner, that is converted to height by the piezo electric calibration factor. Images were collected at -0.2 V vs Cu_{ref} with a tip bias of +0.1 V that correspond to -0.058 V_{NHE} and 0.042 V_{NHE} respectively. The in-plane dimensions of the image cross-sections were scaled to the known nearest neighbor spacing, 0.3615 nm, of the c(2x2) Cl- adlattice. Variations less than 0.01 nm were evident between images. Further details on the microscope and the W STM tip preparation and coating procedures can be found in Ref. 48

Results and Discussion

Step Edge Formation Energies on Cu(100)

A schematic view of the different step edge geometries and chloride coverages considered in this work are shown in Figure 1. On clean vicinal Cu(100) two limiting step configurations were evaluated, straight, kink free $\langle 110 \rangle$ (S₁ Clean) steps and the kink saturated $\langle 100 \rangle$ (S₂ Clean) steps (Figure 1). STM studies of equilibrium island shape indicate the $\langle 110 \rangle$ steps are favored, as coordination is maximized by minimizing the kink density.⁴⁹ Our DFT calculations agree with these experimental observations, predicting larger formation energies for the kinked steps versus the straight steps (0.033 eV/Å vs 0.015 eV/Å).

From a combination of low-energy electron diffraction,⁵⁰ STM,⁸⁻¹⁵ and surface X-ray diffraction³⁴⁻³⁶ experiments, chloride is known to adsorb on Cu(100) surfaces at four-fold

hollow sites as an ordered $c(2 \times 2)$ adlattice structure in both ultrahigh vacuum conditions and at applied potentials greater than $-0.10 V_{SHE}$ in acidic electrolyte. The presence of an ordered $c(2 \times 2)$ halide adlattice on Cu(100) drives step faceting in the $\langle 100 \rangle$ crystallographic directions. These directions correspond to the step orientation of the S_2 clean, S_2 , S'_2 , and $S'_2 + Cl$ steps as shown in Figure 1a and 1b. The Cl stabilizes the steps along the close-packed direction of the halide adlattice (S_2 -type steps), relative to the steps along the close-packed direction of the metal (S_1 -type steps). We use DFT calculations to identify energetically favorable structures that the Cl adlattice will adopt near Cu steps, and predict how the adlattice structures alter the relative stability of S_1 and S_2 steps. We then use our DFT-based BPNN to study the long-range effects of the step structure on the Cl adlattice after assessing its ability to replicate the energetic trends predicted by DFT.

The S_2 and S'_2 steps shown in Figure 1a and 1b feature Cl atoms bound to threefold hollow sites at the edge of the upper terrace. While the atomic positions of the clean surface are clearly defined the occupancy and site geometry of halide atoms at step edges is more challenging to determine. In many models Cl^- is assumed to occupy the four-fold hollow sites with little distortion at the step.^{8-15,51} In two other studies, occupancy of three-fold sites was considered for the S_2 out-of phase steps.^{12,15} However, this assignment was quickly dismissed in the electrochemical study in favor of a four-fold site based on image analysis.¹⁵ When compared against these step structures, our DFT calculations found the structures S_2 and S'_2 in Figure 1b to have more favorable step formation energies. A direct comparison between the 4-fold and 3-fold coordinated structures and their corresponding energies are shown in Figure S1 and S2, respectively. Similar structures have also been proposed for other halide-covered step-edges in Pd-I,¹⁷ Ag-I,¹⁶ and Ni-S systems.⁵²

To demonstrate that our BPNN potential can accurately model Cu(100)- $c(2 \times 2)Cl$ surface facets, we compare step edge formation energies computed with the BPNN against those from the DFT training set. Figure 1c demonstrates that our BPNN calculations capture the step edge formation energy trends present in the DFT calculations. Nearly all of the step

formation energies predicted by the BPNN were within 0.005 eV/Å of their corresponding DFT values. However, the BPNN step formation energy of the $S_1+\text{Cl}$ and $S'_2+\text{Cl}$ steps deviates from the DFT step formation energy by 0.011 and -0.013 eV/Å, respectively. The relatively large error for these formation energies is not surprising because the $S_1+\text{Cl}$ and $S'_2+\text{Cl}$ chloride adlattice structures were discovered using our BPNN and were not included in the initial training set. This demonstrates that the BPNN is capable of predicting the relative energetics of chloride coverages not included in the initial training set, although at potentially reduced accuracy. Including $S'_2+\text{Cl}$ structures in the training set would improve the ability of future BPNNs to model similar chloride adlattice structures and other systems with high chloride coverages. Additional comparison between the BPNN and the DFT training set is available in the supporting information (SI).

The BPNN and DFT results of Figure 1c both indicate that the S'_2 step has the lowest energy at the lowest potentials considered, and as the potential increases, the S_2 step becomes the lowest energy step. At yet higher potentials, the $S'_2+\text{Cl}$ step is predicted to be the lowest energy step, although this has not been experimentally investigated due to the onset of rapid dissolution. For an arbitrary miscut vicinal Cu(100) surface, or a monolayer island, a combination of $\langle 100 \rangle$ steps will exist at a given potential. Due to the nature of the the $c(2\times 2)$ adlattice on adjacent monolayer terraces, two S_2 steps or two S'_2 steps are unlikely to intersect, as this would require a Cl domain wall within the terrace, which would be energetically unfavorable. In contrast, orthogonal S_2 and S'_2 steps can intersect without disrupting the chloride adlattice on the adjacent terraces. The BPNN and DFT step edge energetics reveal the range of potentials where the S_2 and S'_2 steps are the most energetically favorable step edges. We expect from the BPNN results that rectangular islands composed of S_2 and S'_2 steps would form at those potentials, from -0.01 to 0.28 V vs NHE (or from 0.08 to 0.35 V vs NHE according to DFT). Experimentally, rectangular islands of S_2 and S'_2 steps have been commonly observed, although at somewhat lower potentials.

The STM images shown in Figure 2a and 2b show a stepped Cu(100) surface composed of

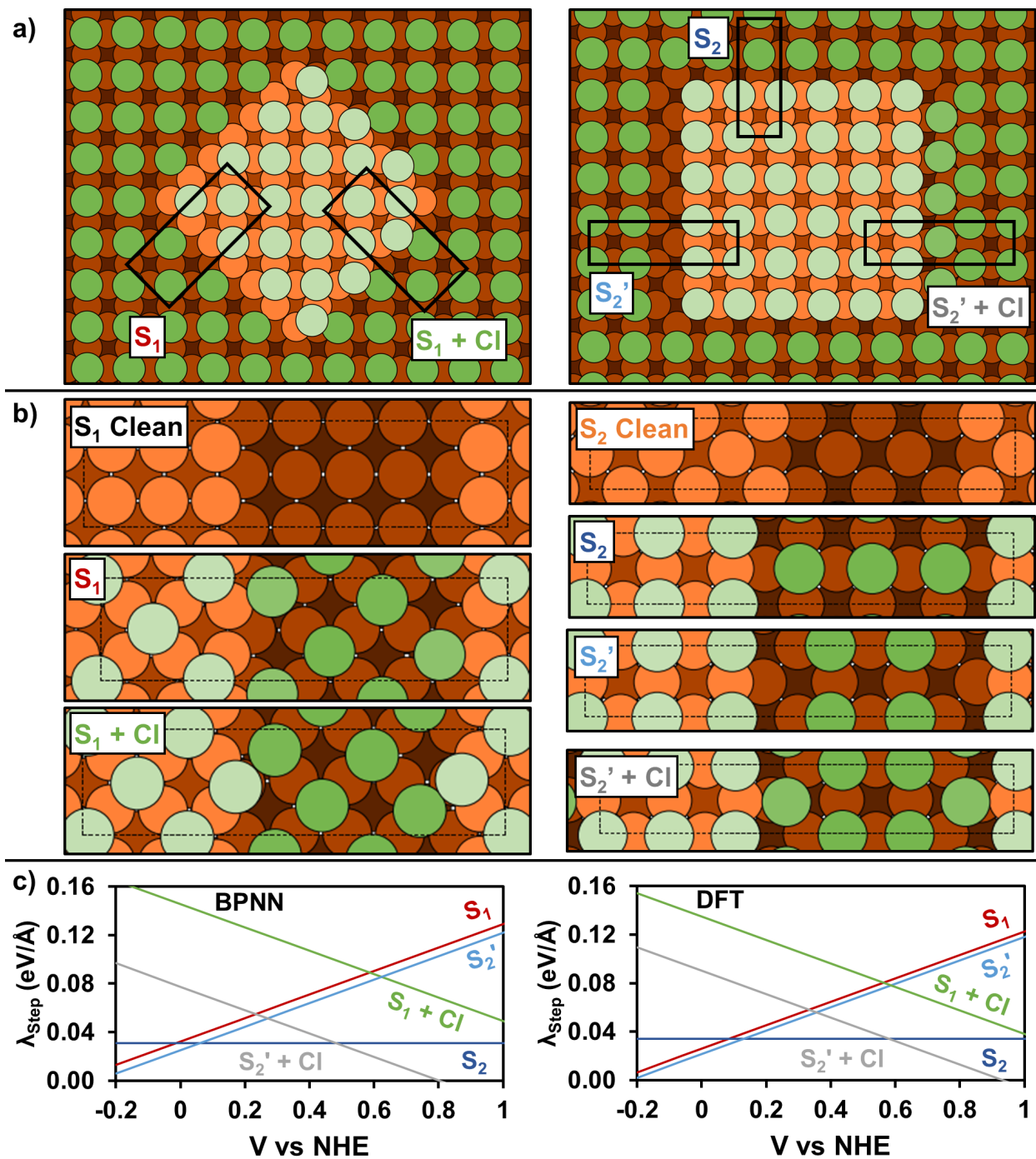


Figure 1: a) Schematics of islands composed of S_1/S_1+Cl steps and $S_2/S_2'/S_2'+Cl$ steps. b) The DFT simulation cells of step edges on the Cu(100) and Cu(100)-c(2x2)Cl surface. c) DFT vs BPNN for step edge energies as a function of potential, using the computational hydrogen electrode approach with DFT unit cells, as defined in the SI.

S'_2 and S_2 steps. Although DFT can be used to model smaller-scale S_2 and S'_2 steps as shown in Figure 1, these surface features are too large to be modeled with DFT. Fortunately, BPNNs can fully optimize the local step structures while maintaining chemical accuracy with respect to DFT. While the BPNN-optimized step structures in Figure 2c and 2d are still smaller than the experimentally observed step, these structures are composed of more than 3000 atoms and would be challenging or impossible to study using DFT and current computational resources. A comparison of the DFT- and BPNN-predicted Cl adsorbate positions and height profile near S_2 steps are shown in Figure S6. While structures this large may not be strictly necessary to characterize monolayer S_1 , S_2 and S'_2 steps, the ability to simulate structures with thousands of atoms can be used in future work to help characterize more complicated surface environments (such as multi-layer steps or screw defects).

The BPNN-predicted height profile of the Cl adlattice agrees with the STM height profile across the out-of-phase and in-phase steps (Figure 2e and 2f) ¹. Figure S6 shows that the peaks on a simulated constant current STM image are centered over the position of the chloride adsorbates supporting the adsorbate assignments. In both the BPNN and STM height profiles, the adsorbate height at the edge of the step is slightly lower than the other adsorbates on that particular terrace. We observe this effect on both the out-of-phase step (Figure 2e) and in-phase steps (Figure 2f). Indeed, close inspection of a selection of previous published images⁸⁻¹⁵ reveal significant indications of distortion at the step edges although limited discussion was offered. From the BPNN-predicted structure, the Cl height at the step corresponds to the Cl positioned in the 3-fold hollow site, rather than in a 4-fold hollow site (See SI Figure S1, S2, and S6).

A slight zig-zig pattern evident in the Cl adlattices shown in Figure 2c and 2d that is produced by Cl atoms binding slightly off-center in the four-fold hollow sites as shown in Figure S7. This structural artifact is due to a shallow potential energy surface for Cl binding. Molecular dynamics simulations at 300K showed that vibrations due to thermal energy result

¹The STM height data at the step edge convolves the sharpness of the step and the STM tip. This constrains the resolution of the lower terrace adjacent to the step as seen in Figure 2e

in the average location of every Cl atom being centered in the four-fold hollow sites as shown in Figure S8, eliminating the Cl adlattice defect.

The DFT derived step formation energies shown in Figure 1c were computed using relatively small unit cells that were limited in size by the computational expense of the calculations. Schematics of the respective unit cell are shown in Figure S1. BPNNs enable us to model long-range structural effects that cannot be captured within these small simulation cells, and determine how step formation energies converge as the system size is increased as illustrated in Figure 3a. Figure 3b and 3c show the long-range behavior of step edges computed with the BPNN, illustrating the larger cell sizes needed to reach convergence. For almost every step geometry, the presence of adsorbed Cl atoms leads to long-range repulsive interactions that are not observed for the clean steps. One exception is the high-coverage S_1 step, S_1+Cl , where we primarily predict attractive interactions between Cl-covered steps. Additionally, the steps disrupt the Cl adlattice structure and this disruption contributes to the long convergence lengths. Analysis of the adlattice disruption is provided in Figure S7. This is consistent with previous reports that adlattice distortion at step edges can cause long-range step-step interactions.⁴⁹ We also note that disruptions to the Cl adlattice are not as significant for the upper terrace, which converges at shorter terrace widths than the lower terrace.

Finally, Figure 3d compares the BPNN step edge formation energies from the smaller unit cells and larger, fully converged cells. The figure demonstrates that some steps such as S_2 are nearly energetically converged at the DFT cell size, while others such as S_1+Cl have larger energy changes. Additionally, we note that the S'_2 step becomes significantly more stable relative to the S_1 step due to these effects.

Cu Dissolution and Electrocrystallization Energetics

Layer-by-layer dissolution and electrocrystallization, mediated by kink propagation, has been experimentally observed on copper surfaces covered with chloride and bromide adlayers.⁸⁻¹⁵

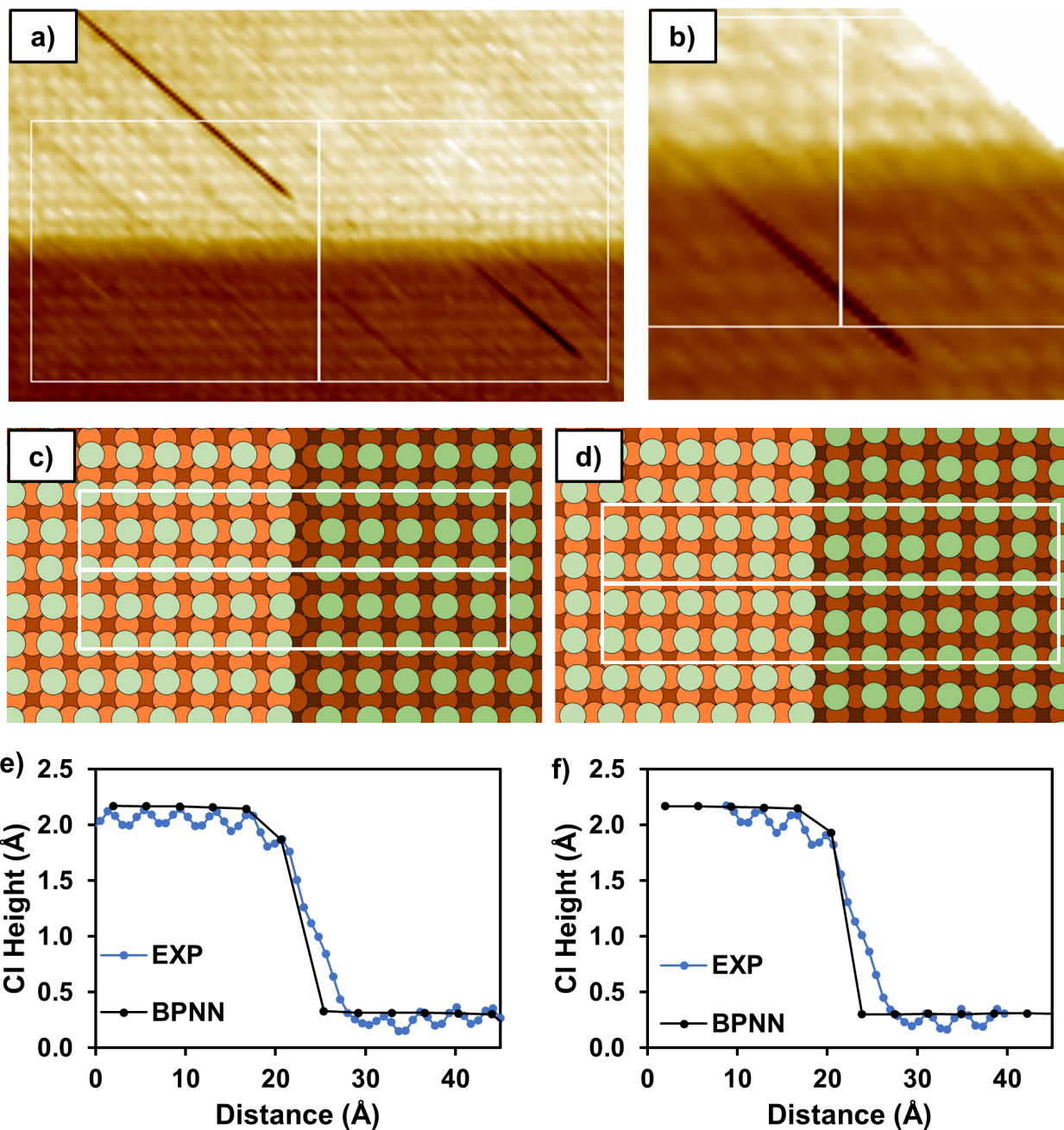


Figure 2: Surface vicinal to Cu(100) with a Cl adlattice, showing multiple steps. STM images of the step with an a) in-phase (S'_2) and b) out-of-phase (S_2) Cl adlattice (white boxes). c) and d) depict BPNN optimized surface structure representing the STM images in a) and b). Comparisons of the BPNN predicted Cl height across and the STM height profile for the e) in-phase step edge and the f) out-of-phase step edge. Simulated STM images of the out-of-phase step are available in Figure S6.

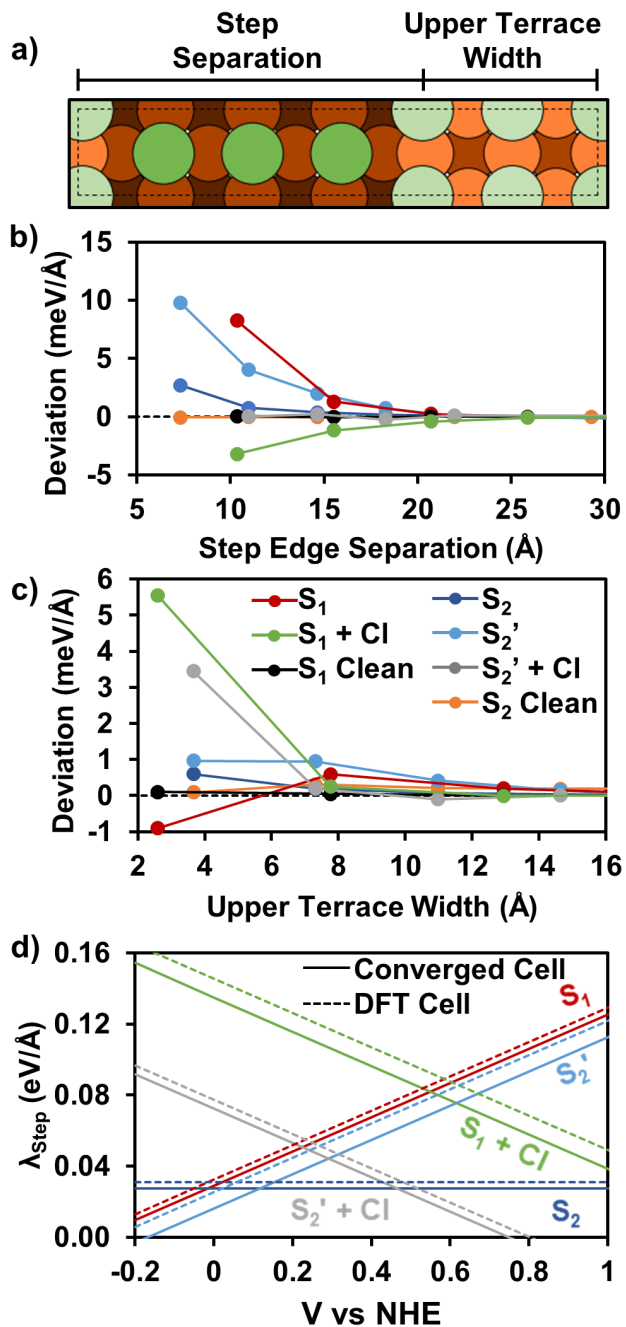


Figure 3: a) Schematic of step edge separation and step width. Deviation from fully converged step formation energies as a function of b) upper and c) lower terrace width. d) comparison between DFT cell and converged step edge formation energies computed with BPNN (See SI for structures).

Similar phenomena are seen broadly for other metal-adsorbate combinations, including Au, Ni, Ag, and Pd surfaces with surface adsorbates including halides and sulfur.^{16,52-56} Uniquely, these processes appear to be primarily controlled by facet-dependant surface thermodynamics, rather than by solution-phase chemistry related to specific product speciation.^{17,57,58}

For Cu(100)-c(2x2)Cl, high-speed STM imaging has shown that dissolution initiates preferentially at corners produced by the intersection of S_2 and S'_2 steps.¹⁴ Dissolution at small overpotentials then preferentially propagates along the S_2 step (out-of-phase) while the S'_2 step (in-phase) does not react. This strongly anisotropic dissolution of S_2/S'_2 rectangular islands has been experimentally measured at applied potentials starting at $-0.07 V_{NHE}$.¹⁴ The anisotropy has been attributed to the difference in adlayer geometry at the respective steps.^{14,16,17,52} These processes appear to occur over length-scales that are too large to be easily modeled with DFT, so these theories had not previously been tested with first-principles based computational methods. We use BPNN potentials to determine how differences in the adlayer structure influence copper atom removal energies and ultimately produce anisotropic dissolution.

Figure 4a shows the corner of a rectangular island composed of S_2 and S'_2 steps. The c(2x2) adlattice is in-phase across the upper and lower terrace at the S'_2 step, and there is a phase shift between the Cl adlattice adsorbed to the upper and lower terraces at the S_2 step. The simulation is periodic in every direction, so structures this large are necessary both to create the appropriate separation between islands in the periodic images and to ensure that dissolution energetics of Cu atoms are not effected by their proximity to other corners or edges of their island. The island consists of more than 3800 atoms, so even though DFT could provide similar insight into the dissolution energetics, it is unlikely that such a calculation could be easily completed with current computational resources.

The dissolution energetics displayed in Figure 4b show that the energy required to remove Cu atoms from the S_2 and S'_2 steps is strongly influenced by the local adlayer structure. As a result of the Cl adlattice phase shift, Cu atoms on the corner of S_2 steps require less energy

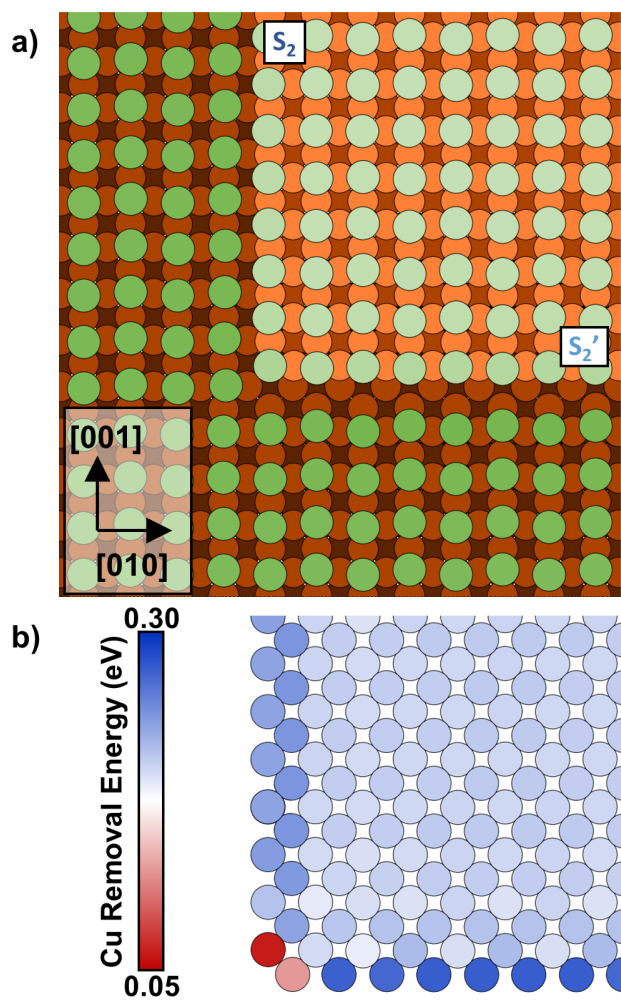


Figure 4: a) schematic of a $c(2 \times 2)$ chloride adlattice on a corner of a copper island composed of S_2 and S_2' steps on a Cu(100) surface. The full simulation cell is twice as large in the x- and y- direction. Arrows denote the labeled crystallographic directions. b) Cu atoms on the island shown in (a), with a superimposed heatmap of the energy required to remove any individual Cu atom, while leaving Cl adsorbed to the surface.

to be removed than atoms on the corner of S'_2 steps. However, the removal of the Cu atom at the corner of the S_2 and S'_2 steps is more energetically favorable than the removal of any other Cu atom from the steps in either crystallographic direction. Our results suggest that the corners produced at intersecting step edges are the favored dissolution site of monolayer islands, congruent with the experimental observations of the onset of dissolution that is synonymous with kink nucleation.¹⁴

Removing the Cu atoms at the corner of the S_2 and S'_2 steps leads to the expansion of an S_1 step that connects the S_2 and S'_2 steps. We removed several rows of Cu atoms to produce the S_2 - S_1 and S_1 - S'_2 intersections shown in Figure 5a. These structures were chosen because they capture the different dissolution energetics that result at the corner of S_2 - S_1 and S_1 - S'_2 intersections that might be transiently produced by the dissolution of the structure shown in Figure 4a. Figure 5b shows that the Cu atoms in the middle of the S_1 step are more susceptible toward dissolution than atoms along the S_2 or S'_2 steps, but the Cu atom labeled "a" at the S_2 - S_1 intersection is the most susceptible. The calculated energies to remove the Cu atoms in Figure 5b are shown in Figure 5c. Removing Cu atoms from the S_2 - S_1 and S'_2 - S_1 corners shows that the newly exposed corner atoms, that define a kink, exhibit approximately the same driving force for dissolution as the corner atoms that were removed. Pairs of Cu atoms are removed from the S_2 - S_1 and S'_2 - S_1 corners in Figure 5b because the removal of a second Cu atom from both corners (atoms b, g, j, and k) was 0.1 to 0.2 eV more favorable after the first atom was removed from each corner (atoms a, h, i, and l) as shown in Figure S10. This prediction, that it is more energetically favorable to remove Cu atoms from S_2 - S_1 corners than from S'_2 - S_1 corners, is qualitatively consistent with the reported experimental dissolution trends.¹⁴

The presence of the phase shift between the Cl atoms adsorbed to the upper and lower terrace causes the Cu atoms at the S_2 - S_1 intersections (atoms a, i/c, and m/c) to have a removal energy that is 0.06 eV more favorable than Cu atoms at the S'_2 - S_1 intersections (atoms h, f/l, and f/p). Based on the Brønsted-Evans-Polanyi principle, this energy difference

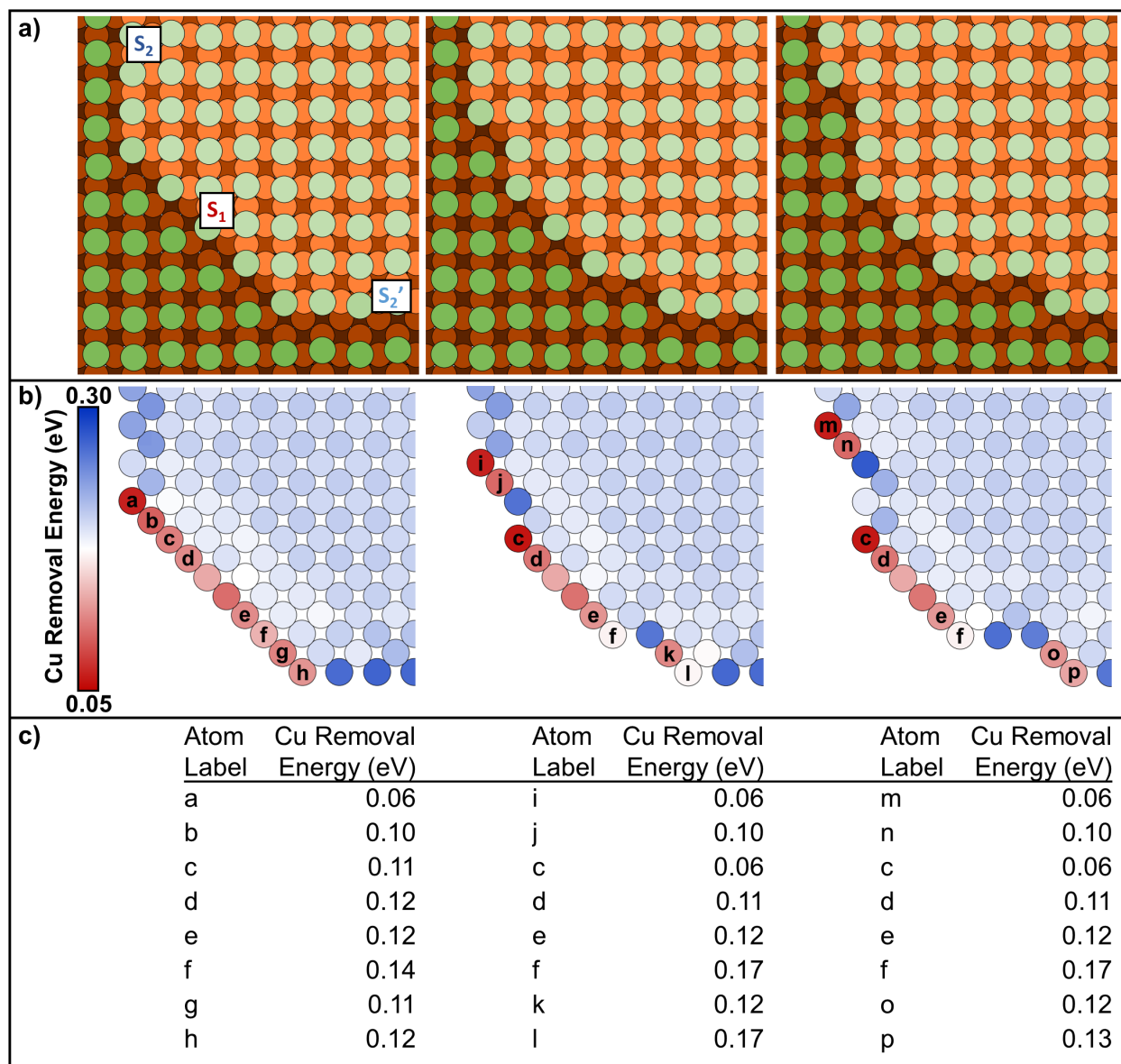


Figure 5: a) schematic of copper dissolution occurring at the intersection of S_2 - S_1 , and S_1 - S_2' steps on a copper monolayer step island covered in Cl. The left panel shows the pristine steps. The middle and right panels show the island with two Cu atoms removed from both the S_2 and S_2' steps (See SI for the intermediate steps). b) heatmaps of the energy required to remove any individual Cu atom from the islands shown in (a) while leaving Cl adsorbed to the surface. Adsorbed Cl is not shown for clarity. c) removal energies for atoms labeled in b

would result in kink generation and propagation proceeding approximately 10 times faster along the S_2 step than along the S'_2 step according to the Butler-Volmer equation. Removing Cu atoms from the step edge reveals new S_2 or S'_2 steps. The atoms at the kink positions represent the dominant site of dissolution. Combining these energetics with the fact that removing Cu atoms from the center of the upper terrace is significantly uphill in energy, leads us to believe that dissolution primarily occurs at the corner of Cu islands and its propagation results in layer-by-layer removal of Cu. No pitting is likely to occur on otherwise flat terraces unless the overpotential is significantly increased.

Conclusions

We have investigated how the Cl adlayer on surfaces vicinal to Cu(100) impacts the relative step stabilities, and found that our model predicts step stability trends consistent with experimental observations. Our DFT calculations show that for the bare copper surface S_1 steps are lower in energy than S_2 steps, but the $c(2 \times 2)$ chloride adlattice reverses this trend and favors the formation of S_2 steps. We have trained a BPNN potential that is chemically accurate with respect to our initial DFT calculations (energy errors < 5 meV/atom, force errors < 60 meV/Å). Our final BPNN potential can reproduce step edge formation energy trends predicted by DFT calculations. Notably, any BPNN calculation can be completed with significantly less computational resources than required by the analogous DFT calculation. This enabled us to study the structure and energetics of surface facets that were far larger than could be modeled with DFT alone.

Surprisingly, both the DFT and BPNN calculations predict that S_2 and S'_2 steps have lower step formation energies when Cl adsorbed at the edge of the upper terrace occupies a three-fold hollow site, as opposed to a four-fold hollow site as previously suggested in the literature. The three-fold hollow chloride binding at these steps is further supported by the height profile variations at the edge of S_2 and S'_2 steps in STM images.

The Cl adlayer mediates layer-by-layer, anisotropic dissolution of copper surfaces. Our BPNN calculations determined that dissolution of monolayer, rectangular copper islands on Cu(100)-c(2x2)Cl initiates at the corner of islands, creating a kink which then propagates down S_2 steps. The energetics of kink propagation are dependent on the phase relationships of the Cl at the respective steps. This dissolution process is driven by energetic differences produced by out-of-phase (S_2) and in-phase (S'_2) Cl step geometries that result from the long-range order of the Cl adlayer. We note that the reverse process may also operate as an electrocrystallization mechanism, a possible topic for future work.

These results demonstrate that the BPNN simulations can guide the interpretation of experimental structural data at length-scales longer than what can be modeled with DFT. This work could be extended to investigate the structural evolution of other adsorbate-covered surfaces and nanoparticles. The key insights provided by our BPNN simulations help improve our understanding of the factors that guide adsorbate-templated surface growth and dissolution, two processes that control the structural evolution for a variety of metal-adsorbate systems.

Associated Content

Supporting Information

The supporting information is available free of charge at pubs.acs.org.

- Additional computational results and the Behler-Parrinello neural network benchmarking results.
- A compressed file containing the training, test, and validation sets used to train the Behler-Parrinello neural network presented here.

Author Information

Corresponding Author

*E-mail: mitchell.groenenboom@nist.gov

Notes

The authors declare no competing financial interests.

Acknowledgements

- The authors have no external funding source to disclose.

References

- (1) Fukushima, T.; Nishio, K.; Masuda, H. Inkjet printing for site-controlled tunnel pitting with high aspect ratio in al. *Electrochem. Solid-State Lett.* **2010**, *13*, C9–C11.
- (2) Frankel, G. S.; Li, T.; Scully, J. R. Localized corrosion: Passive film breakdown vs pit growth stability. *J. Electrochem. Soc.* **2017**, *164*, C180–C181.
- (3) Marcus, P.; Maurice, V. Atomic level characterization in corrosion studies. *Philos. Trans. R. Soc. A* **2017**, *375*, 20160414.
- (4) Xia, Y.; Xiong, Y.; Lim, B.; Skrabalak, S. E. Shape-controlled synthesis of metal nanocrystals: Simple chemistry meets complex physics? *Angew. Chem. Int. Ed.* **2009**, *48*, 60–103.
- (5) Meena, S. K.; Sulpizi, M. From gold nanoseeds to nanorods: The microscopic origin of the anisotropic growth. *Angew. Chem.* **2016**, *128*, 12139–12143.

- (6) Ghosh, S.; Manna, L. The many "facets" of halide ions in the chemistry of colloidal inorganic nanocrystals. *Chem. Rev.* **2018**, *118*, 7804–7864.
- (7) Moffat, T. P.; Wheeler, D.; Edelstein, M. D.; Josell, D. Superconformal film growth: Mechanism and quantification. *IBM J. Res. Dev.* **2005**, *49*, 19–36.
- (8) Suggs, D. W.; Bard, A. J. Scanning tunneling microscopic study with atomic resolution of the dissolution of Cu(100) electrodes in aqueous chloride media. *J. Phys. Chem.* **1995**, *99*, 8349–8355.
- (9) T.P.Moffat, An in situ STM study of Cu and Ni electrodeposition. *Mat. Res. Soc. Symp. Proc.* **1996**, *404*, 3–8.
- (10) Vogt, M. R.; Möller, F. A.; Schilz, C. M.; Magnussen, O. M.; Behm, R. J. Adsorbate-induced step faceting of Cu(100) electrodes in HCl. *Surf. Sci.* **1996**, *367*, L33–L41.
- (11) Vogt, M. R.; Lachenwitzer, A.; Magnussen, O. M.; Behm, R. J. In-situ STM study of the initial stages of corrosion of Cu(100) electrodes in sulfuric and hydrochloric acid solution. *Surf. Sci.* **1998**, *399*, 49–69.
- (12) Nakakura, C.; Zheng, G.; Altman, E. Atomic-scale mechanisms of the halogenation of Cu(100). *Surf. Sci.* **1998**, *401*, 173–184.
- (13) Broekmann, P.; Anastasescu, M.; Spaenig, A.; Lisowski, W.; Wandelt, K. Atomic structures and dynamics of a Cu(100) electrode in dilute hydrobromic acid: An in situ STM study. *J. Electroanal. Chem.* **2001**, *500*, 241–254.
- (14) Magnussen, O.; Zitzler, L.; Gleich, B.; Vogt, M.; Behm, R. In-situ atomic-scale studies of the mechanisms and dynamics of metal dissolution by high-speed STM. *Electrochim. Acta* **2001**, *46*, 3725–3733.
- (15) Polewska, W.; Behm, R. J.; Magnussen, O. M. In-situ video-STM studies of Cu electrodeposition on Cu(100) in HCl solution. *Electrochim. Acta* **2003**, *48*, 2915–2921.

- (16) Teshima, T.; Ogaki, K.; Itaya, K. Effect of adsorbed iodine on the dissolution and deposition reactions of Ag(100): Studies by in situ STM. *J. Phys. Chem. B* **1997**, *101*, 2046–2053.
- (17) Sashikata, K.; Matsui, Y.; Itaya, K.; Soriaga, M. P. Adsorbed-iodine-catalyzed dissolution of Pd single-crystal electrodes: Studies by electrochemical scanning tunneling microscopy. *J. Phys. Chem.* **1996**, *100*, 20027–20034.
- (18) Suzuki, T.; Yamada, T.; Itaya, K. In situ electrochemical scanning tunneling microscopy of Ni(III), Ni(100), and sulfur-modified Ni(100) in acidic solution. *J. Phys. Chem.* **1996**, *100*, 8954–8961.
- (19) Behler, J. Neural network potential-energy surfaces in chemistry: a tool for large-scale simulations. *Phys. Chem. Chem. Phys.* **2011**, *13*, 17930–17955.
- (20) Bernstein, N.; Csányi, G.; Deringer, V. L. De novo exploration and self-guided learning of potential-energy surfaces. *NPJ Comput. Mater.* **2019**, *5*, 99.
- (21) Gastegger, M.; Schwiedrzik, L.; Bittermann, M.; Berzsenyi, F.; Marquetand, P. WACSF - Weighted atom-centered symmetry functions as descriptors in machine learning potentials. *J. Chem. Phys.* **2018**, *148*, 241709.
- (22) Khorshidi, A.; Peterson, A. A. Amp: A modular approach to machine learning in atomistic simulations. *Comput. Phys. Commun.* **2016**, *207*, 310–324.
- (23) Singraber, A.; Behler, J.; Dellago, C. Library-based LAMMPS implementation of high-dimensional neural network potentials. *J. Chem. Theory Comput.* **2019**, *15*, 1827–1840.
- (24) Kolb, B.; Lentz, L. C.; Kolpak, A. M. Discovering charge density functionals and structure-property relationships with PROPhet: A general framework for coupling machine learning and first-principles methods. *Sci. Rep.* **2017**, *7*, 1192.

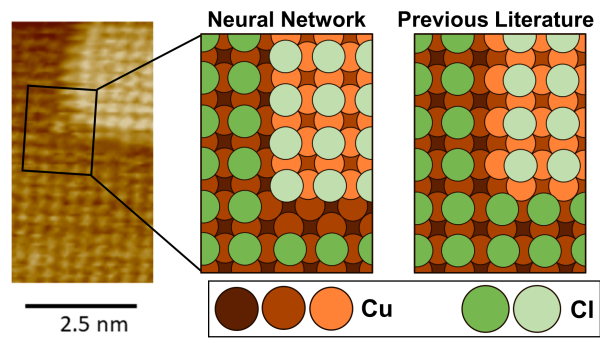
- (25) Artrith, N.; Urban, A. An implementation of artificial neural-network potentials for atomistic materials simulations: Performance for TiO₂. *Comput. Mater. Sci.* **2016**, *114*, 135–150.
- (26) Artrith, N.; Urban, A.; Ceder, G. Efficient and accurate machine-learning interpolation of atomic energies in compositions with many species. *Phys. Rev. B* **2017**, *96*, 014112.
- (27) Natarajan, S. K.; Behler, J. Neural network molecular dynamics simulations of solid-liquid interfaces: Water at low-index copper surfaces. *Phys. Chem. Chem. Phys.* **2016**, *18*, 28704–28725.
- (28) Hellström, M.; Quaranta, V.; Behler, J. One-dimensional vs. two-dimensional proton transport processes at solid–liquid zinc-oxide–water interfaces. *Chem. Sci* **2019**, *10*, 1232–1243.
- (29) Artrith, N.; Morawietz, T.; Behler, J. High-dimensional neural-network potentials for multicomponent systems: Applications to zinc oxide. *Phys. Rev. B* **2011**, *83*, 153101.
- (30) Singraber, A.; Morawietz, T.; Behler, J.; Dellago, C. Parallel multistream training of high-dimensional neural network potentials. *J. Chem. Theory Comput.* **2019**, *15*, 3075–3092.
- (31) Giannozzi, P.; Baroni, S.; Bonini, N.; Calandra, M.; Car, R.; Cavazzoni, C.; Ceresoli, D.; Chiarotti, G. L.; Cococcioni, M.; Dabo, I. et al. QUANTUM ESPRESSO: a modular and open-source software project for quantum simulations of materials. *J. Phys. Condens. Matter* **2009**, *21*, 395502.
- (32) Giannozzi, P.; Andreussi, O.; Brumme, T.; Bunau, O.; Buongiorno Nardelli, M.; Calandra, M.; Car, R.; Cavazzoni, C.; Ceresoli, D.; Cococcioni, M. et al. Advanced capabilities for materials modelling with Quantum ESPRESSO. *J. Phys. Condens. Matter* **2017**, *29*, 465901.

- (33) Zhang, Y.; Yang, W. Comment on 'generalized gradient approximation made simple'. *Phys. Rev. Lett.* **1998**, *80*, 890.
- (34) Gründer, Y.; Kaminski, D.; Golks, F.; Krug, K.; Stettner, J.; Magnussen, O. M.; Franke, A.; Stremme, J.; Pehlke, E. Reversal of chloride-induced Cu(001) subsurface buckling in the electrochemical environment: An in situ surface x-ray diffraction and density functional theory study. *Phys. Rev. B* **2010**, *81*, 174114.
- (35) Keller, H.; Saracino, M.; Nguyen, H. M.; Huynh, T. M. T.; Broekmann, P. Competitive anion/water and cation/water interactions at electrified copper/electrolyte interfaces probed by in situ X-ray diffraction. *J. Phys. Chem. C* **2012**, *116*, 11068–11076.
- (36) Keller, H.; Saracino, M.; Nguyen, H. M. T.; Broekmann, P. Templating the near-surface liquid electrolyte: In situ surface x-ray diffraction study on anion/cation interactions at electrified interfaces. *Phys. Rev. B* **2010**, *82*, 245425.
- (37) Grisafi, A.; Ceriotti, M. Incorporating long-range physics in atomic-scale machine learning. *J. Chem. Phys.* **2019**, *151*, 204105.
- (38) Hjorth Larsen, A.; Jørgen Mortensen, J.; Blomqvist, J.; Castelli, I. E.; Christensen, R.; Dułak, M.; Friis, J.; Groves, M. N.; Hammer, B.; Hargus, C. et al. The atomic simulation environment—a Python library for working with atoms. *J. Phys. Condens. Matter* **2017**, *29*, 273002.
- (39) Plimpton, S. Fast parallel algorithms for short-range molecular dynamics. *J. Comput. Phys.* **1995**, *117*, 1–19.
- (40) Behler, J. Atom-centered symmetry functions for constructing high-dimensional neural network potentials. *J. Chem. Phys.* **2011**, *134*, 074106.
- (41) McCrum, I. T.; Akhade, S. A.; Janik, M. J. Electrochemical specific adsorption of

- halides on Cu 111, 100, and 211: A Density Functional Theory study. *Electrochim. Acta* **2015**, *173*, 302–309.
- (42) Atkins, P. *Physical Chemistry*, 6th ed.; W.H. Freeman and Company: New York, 1997; p 153.
- (43) Yu, B.; Scheffler, M. Ab initio study of step formation and self-diffusion on Ag(100). *Phys. Rev. B* **1996**, *55*, 13916–13924.
- (44) Nørskov, J. K.; Rossmeisl, J.; Logadottir, A.; Lindqvist, L.; Kitchin, J. R.; Bligaard, T.; Jónsson, H. Origin of the overpotential for oxygen reduction at a fuel-cell cathode. *J. Phys. Chem. B* **2004**, *108*, 17886–17892.
- (45) Roques, J.; Anderson, A. B. Electrode potential-dependent stages in OH ads formation on the Pt₃Cr Alloy (111) Surface. *J. Electrochem. Soc.* **2004**, E340–E347.
- (46) Jinnouchi, R.; Toyoda, E.; Hatanaka, T.; Morimoto, Y. First principles calculations on site-dependent dissolution potentials of supported and unsupported Pt particles. *J. Phys. Chem C* **2010**, 17557–17568.
- (47) Nagy, K. S.; Kazemiabnavi, S.; Thornton, K.; Siegel, D. J. Thermodynamic overpotentials and nucleation rates for electrodeposition on metal anodes. *ACS Appl. Mater. Interfaces* **2019**, *11*, 7954–7964.
- (48) Moffat, T.; Yang, L.-Y. O. Accelerator surface phase associated with superconformal Cu electrodeposition. *J. Electrochem. Soc.* **2010**, *157*, D228–D241.
- (49) Giesen, M. Step and island dynamics at solid/vacuum and solid/liquid interfaces. *Prog. Surf. Sci.* **2001**, *68*, 1–153.
- (50) Puisto, M.; Pussi, K.; Alatalo, M.; Hesp, D.; Dhanak, V. R.; Lucas, C. A.; Grunder, Y. LEED – IV and DFT study of the co-adsorption of chlorine and water on Cu(100). *Surf. Sci.* **2017**, *657*, 51–57.

- (51) Van Dijk, F. R.; Zandvliet, H. J.; Poelsema, B. Energetics and dynamics of Cu(001)-c(2x2)Cl steps. *J. Appl. Phys* **2006**, *99*, 123506.
- (52) Ando, S.; Suzuki, T.; Itaya, K. Layer-by-layer anodic dissolution of sulfur-modified Ni(100) electrodes: in situ scanning tunneling microscopy. *J. Electroanal. Chem.* **1996**, *412*, 139–146.
- (53) Kasian, O.; Kulyk, N.; Mingers, A.; Zeradjanin, A. R.; Mayrhofer, K. J.; Cherevko, S. Electrochemical dissolution of gold in presence of chloride and bromide traces studied by on-line electrochemical inductively coupled plasma mass spectrometry. *Electrochim. Acta* **2016**, *222*, 1056–1063.
- (54) Suggs, D. W.; Bard, A. J. Scanning tunneling microscopic study with atomic resolution of the dissolution of Cu(III) in aqueous chloride solutions. *J. Am. Chem. Soc.* **1994**, *116*, 10725–10733.
- (55) McBride, J.; Soriaga, M. Adsorbate-catalyzed corrosion: Anodic dissolution of palladium catalyzed by chemisorbed iodine in halide-free acid solutions. *J. Electroanal. Chem.* **1989**, *303*, 255–259.
- (56) Müller, P.; Ando, S.; Yamada, T.; Itaya, K. Formation of an ordered structure of iodine adsorbed on Ni(111) and the anodic dissolution processes: in-situ STM study. *J. Electroanal. Chem.* **1999**, *467*, 282–290.
- (57) Soriaga, M.; Schimpf, J.; Carrasquillo, A.; Abreu, J.; Temesghen, W.; Barriga, R.; Jeng, J.-J.; Sashikata, K.; Itaya, K. Electrochemistry of the I-on-Pd single-crystal interface: studies by UHV-EC and in situ STM. *Surf. Sci.* **1995**, *335*, 273–280.
- (58) Temesghen, W. F.; Abreu, J. B.; Barriga, R. J.; Lafferty, E. A.; Soriaga, M. P.; Sashikata, K.; Itaya, K. Anodic dissolution and reordering of Pd(110) induced by chemisorbed iodine. *Surf. Sci.* **1997**, *385*, 336–345.

TOC Graphic



Supporting information for Halide-induced Step Faceting and Dissolution Energetics from Atomistic Machine Learned Potentials on Cu(100)

Mitchell C. Groenenboom, Thomas P. Moffat, and Kathleen A. Schwarz

Material Measurement Laboratory

National Institute of Standards and Technology

Gaithersburg, MD 20899-8520 USA

Step Edge Structure

Chloride ions form a saturated $c(2 \times 2)$ adlattice when bound to Cu(100) terraces. In this adlattice structure, the Cl atoms prefer to maximize their coordination to the surface and bind to four-fold hollow sites. In several prior studies it has previously been assumed that the adlattice structure near steps in the $\langle 100 \rangle$ crystallographic direction occupied four-fold hollow sites up to the edge of the step, as shown in Figure S1c and S1e. Alternative step structures with chloride ions bound to three-fold hollow sites are shown in Figure S1b and S1d. The majority of Cl ions remain bound in four-fold hollow sites, and only the adsorbates near the edge of the upper terrace have a different coordination environment.

We compare the step formation energy of S_2 and S'_2 steps with Cl bound to four-fold (Figure S1c and S1e) and three-fold (Figure S1b and S1d) sites in Figure S2. Both the S_2 and S'_2 steps have lower step formation energies when Cl near the edge of the upper terrace is bound to a three-fold hollow site in contrast to prior assumptions.

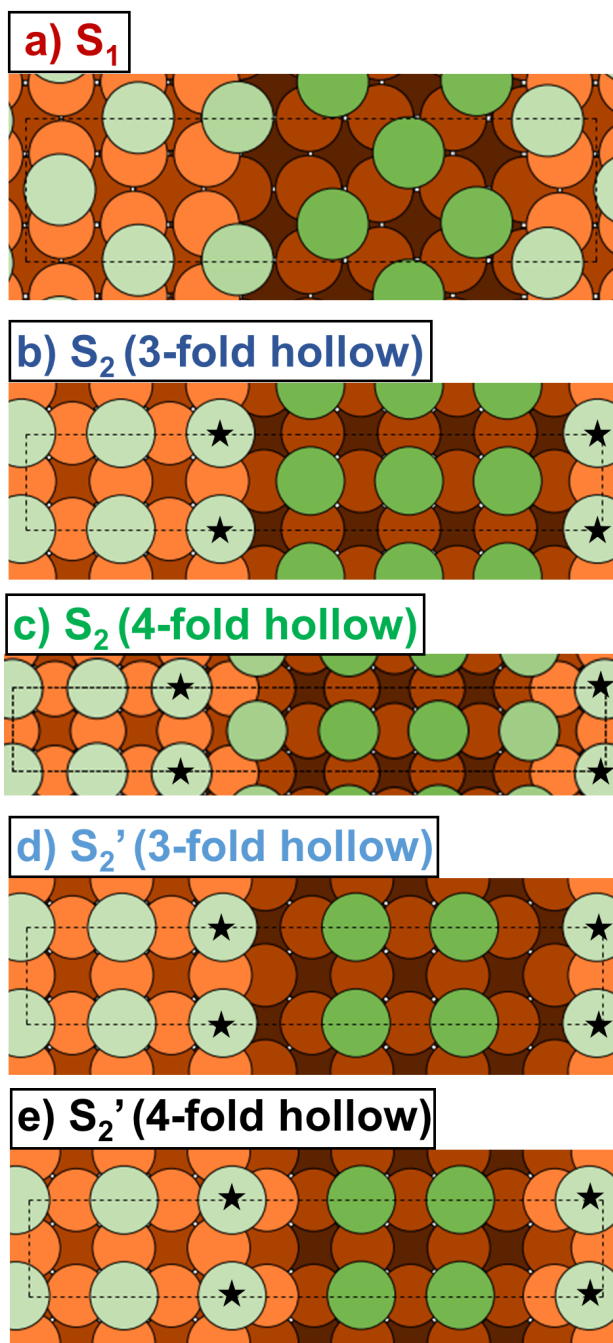


Figure S1: Optimized DFT simulation cells containing the S_1 , S_2 , and S_2' step structures. S_2 , and S_2' are shown with Cl atoms (labeled with stars) at the edge of the upper terrace bound in either 3-fold or 4-fold hollow sites.

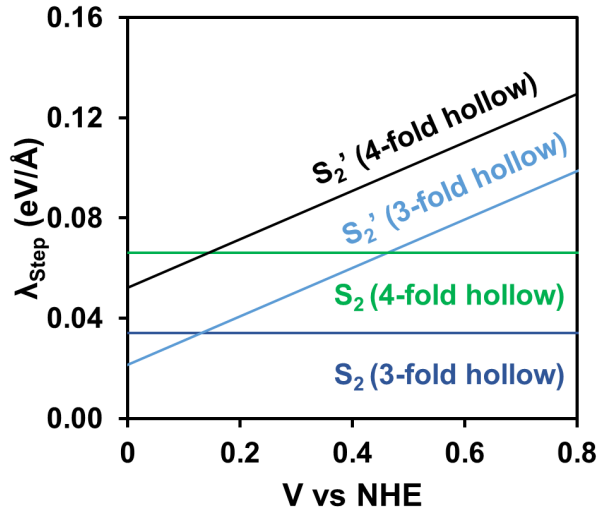


Figure S2: Step edge formation energies of the S_2 , and S'_2 steps shown in Figure S1.

Evaluating BPNN Accuracy

We trained our Behler-Parrinello neural network (BPNN) according to the procedure described in the main text. Figure S3 shows the energy and force RMSE of our BPNN over 25 training epochs. Despite some oscillations in the energy RMSE during the early training epochs, the BPNN appears fully converged after approximately 20 epochs. We selected the BPNN parameters from training epoch 22 as our final BPNN. This parameter set had comparable energy and force RMSE values for both the training and test sets, suggesting that our BPNN is not overfit to the training data.

Figure S4 shows the distribution of errors for the BPNN calculated energy of every structure in the training, test, and validation set. Over a wide-range of DFT energies, the BPNN errors are consistently smaller than our convergence criteria (5 meV/atom). Of the 900 structures in our dataset, only six structures (five from the training set and one from the test set) have energy errors larger than 5 meV/atom. The training, test, and validation sets have similar overall error distributions, which seems to confirm that our BPNN is not overfit to the training data. Although the overall energy RMSE is relatively small, the error distribution shows that there is a systematic error of 1.6 meV/atom. Eliminating this systematic error would further increase the accuracy of our BPNN potential with respect to

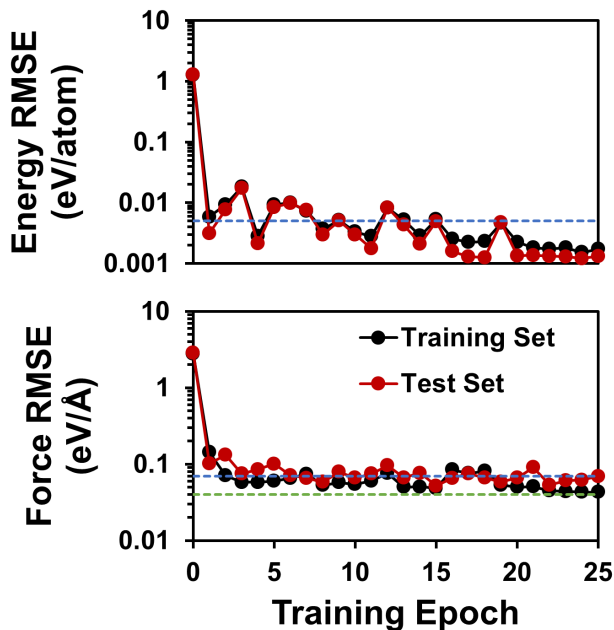


Figure S3: Comparing the BPNN predicted energies and forces against the DFT values present in the training and test sets per BPNN training epoch. The dashed lines correspond to our convergence criteria (5 meV/atom for the energy RMSE, and 4 - 7 eV/Å for the force RMSE).

our DFT calculations.

Figure S5 shows the distribution of errors for the BPNN calculated forces acting on every atom in every structure in the training, test, and validation set. While Figure S4 compares the energies of all 900 structures in our dataset, Figure S5 compares more than 180,000 atomic forces. A number of forces have errors that are larger than our force convergence criteria (80 meV/Å), but the error distribution of the training, test, and validation sets show that these outliers are a relatively small percentage of the total set of atomic force calculations. The majority of atomic forces are predicted within 80 meV/Å. The error distribution of the training, test, and validation sets are similar, suggesting that our BPNN does not appear to be overfit to the training data.

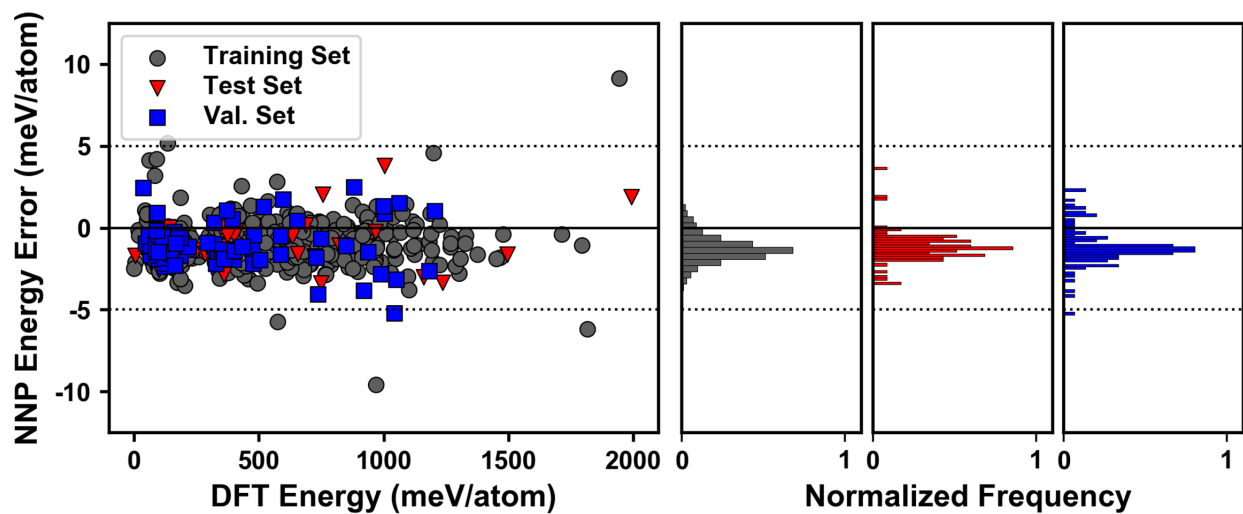


Figure S4: The distribution of BPNN errors over a range of DFT computed energies. The dashed lines correspond to errors of ± 5 meV/atom.

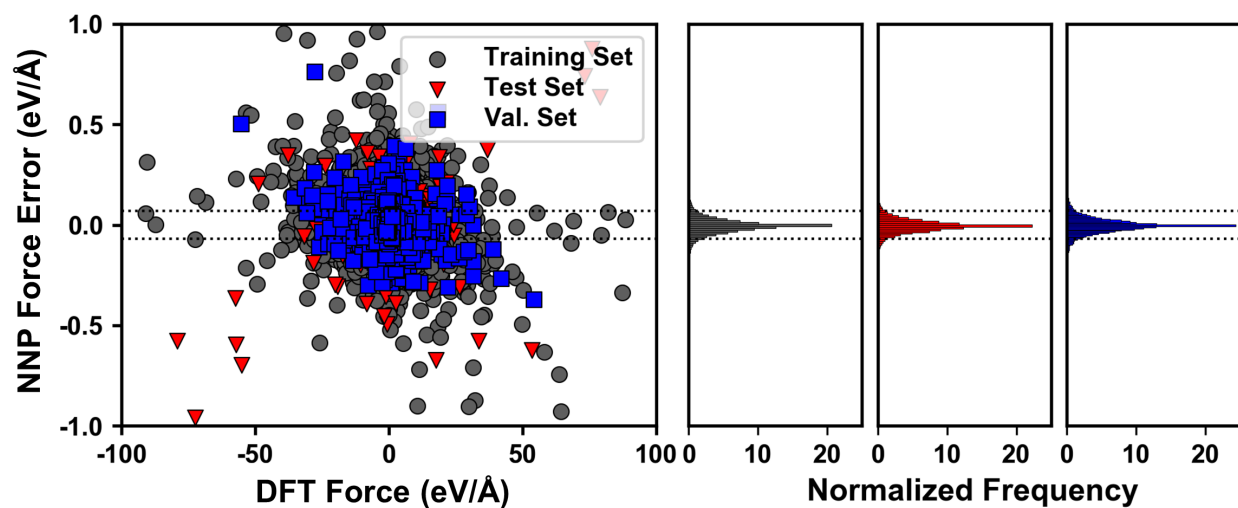


Figure S5: The distribution of BPNN errors over a range of DFT computed atomic forces. The dashed lines correspond to errors of ± 70 meV/Å.

Simulated STM image

We generated simulated constant current STM images of the S_2 step structure shown in Figure S1b. The simulated STM image was generated using Quantum Espresso following the procedure that is available in Quantum Espresso documentation. First, we performed an SCF calculation using the parameters described in the main text. We then performed an NSCF calculation with 25% additional bands than required for the number of electrons in the calculation and twice as many k-points in the x and y directions (a $2 \times 16 \times 1$ k-point grid). We then used the PostProc Quantum Espresso module to calculate the constant current STM height profile. The image shown here uses a tip bias of -0.2721 V and a density isovalue of 1×10^{-5} . The SCF and NSCF calculations were performed on the unit cell shown in Figure S1b and the unit cell was replicated three times vertically to help visualize the electron density at the steps.

The STM image (Figure S6b) shows that the peaks of the electron density are located nearly directly over the atomic position of the chloride atoms adsorbed to the upper and lower terraces of the steps (Figure S6a). Comparing the height profiles in Figure S6c yields three clear observations. First, the scaled STM height trends agree between the experimental and calculated STM images. Second, the heights of the Cl atoms in the DFT structure match the heights predicted by the BPNN. Finally, the height profile of the simulated STM image matches that of the DFT structure. These findings suggest that the STM heights correlate well with the adsorbate positions of Cl adsorbates on Cu(100), and that our BPNN is accurately reproducing the DFT determined adsorbate locations near S_2 steps. While DFT can be used to verify the structure of simple steps (such as the S_1 and S_2 monolayer steps presented in this work), more complex step structures may be too large to be captured in a DFT simulation cell. BPNNs may be used to help guide the interpretation of surface structures, surface dynamics, and adsorption patterns for these cases.

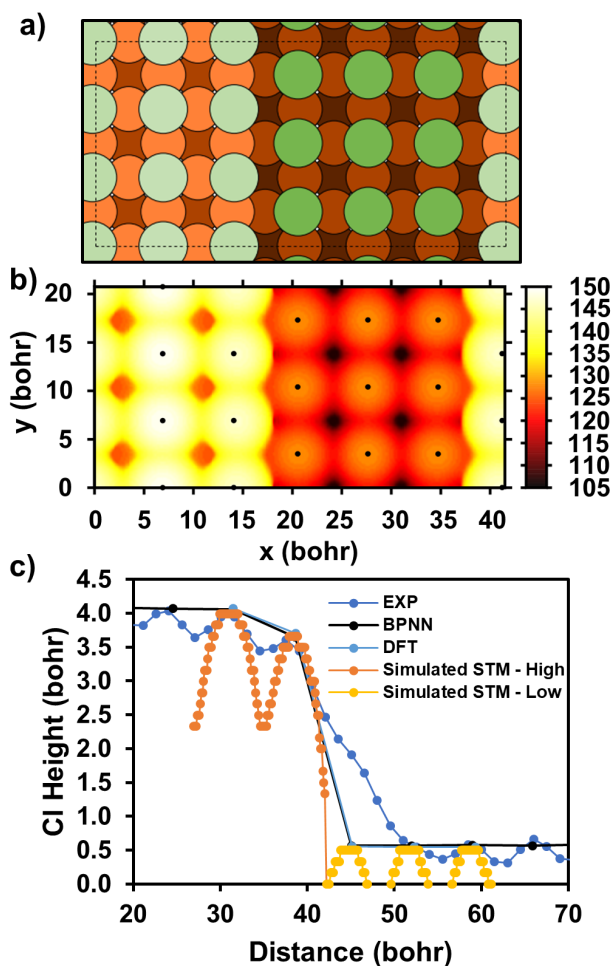


Figure S6: a) Schematic of an S_2 step. b) A constant current STM image of the S_2 step simulated with DFT. The black points correspond to the atomic positions of the chloride adsorbates. c) A comparison of the experimental STM, BPNN, DFT, and simulated STM height profiles. The simulated STM profile is composed of two traces that pass over the peaks of the Cl atoms on the upper and lower terraces. The STM height profiles were scaled to the DFT and BPNN height profiles.

Cl adlattice deviations near steps

Chlorides bind to four-fold hollow sites on Cu(100) terraces. Figure S7 shows that the chlorides on the lower terrace bind slightly off-center near the step edge. The magnitude of this offset decreases further away from the step, and is completely eliminated by the 3rd or 4th chloride. The negatively charged chlorides repel each other, and the adlattice attempts to expand to occupy all available space. This expansion contributes to step-step repulsion.

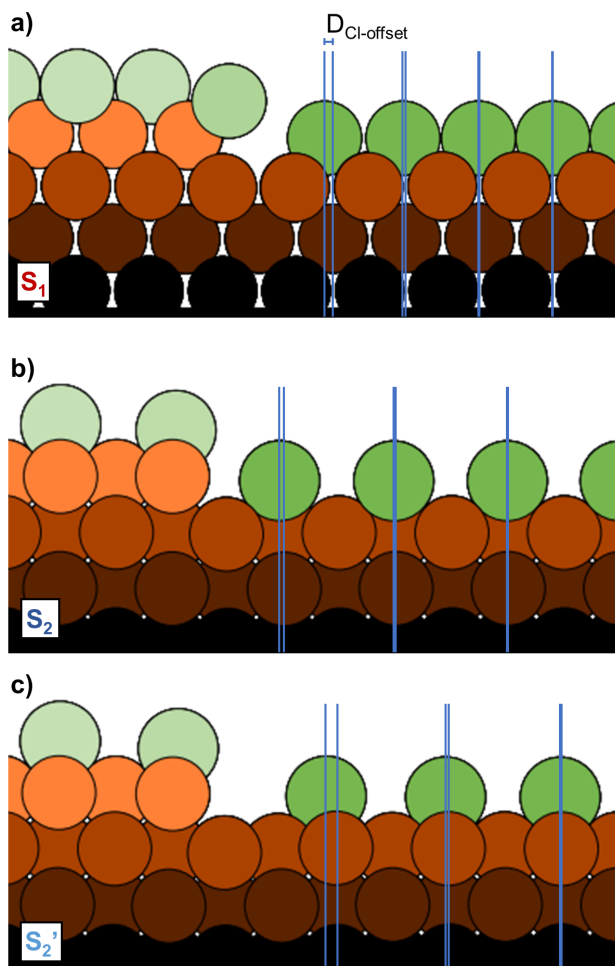


Figure S7: Deviations in the chloride position near a) S_1 , b) S_2 , and c) S_2' steps.

Average position of the Cl adlattice

Optimized structures containing S_2 and S'_2 steps featured a structural anomaly where Cl atoms were not adsorbed to the center of the 4-fold hollow sites. The off-centered arrangement produced a zig-zag pattern in the chloride adlattice. This structural defect is due to a shallow potential energy surface for the Cl binding location. Averaging the position of every Cl atom from an MD trajectory showed that the zig-zag pattern is washed out by the vibrations that result from the thermal energy at 300 K, as shown in Figure S8.

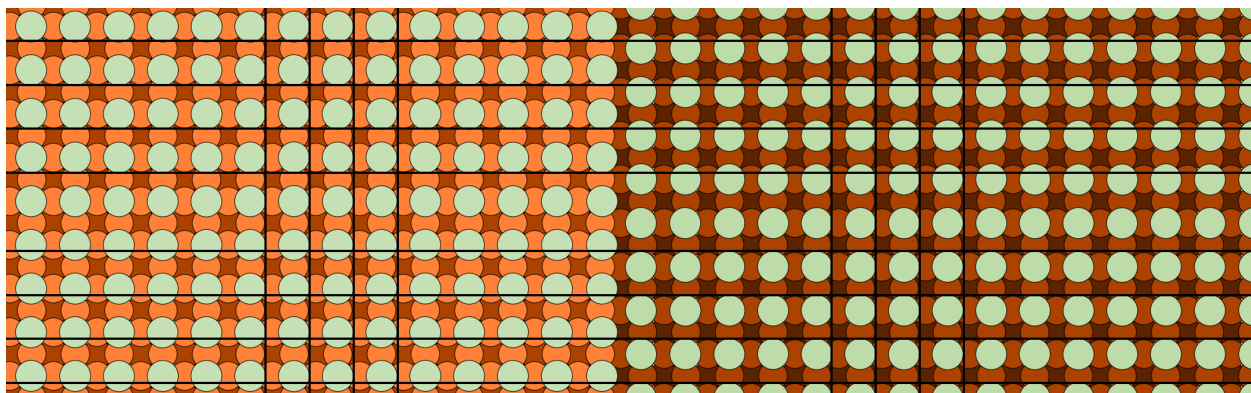


Figure S8: The average positions of atoms from a 100 ps MD trajectory carried out at 300 K. The black lines serve as a visual reference point for the Cl positions on the upper and lower terrace.

Cu dissolution

We model copper dissolution from S_2 and S'_2 steps according to the process shown in Figure S9.

A copper atom is removed from the corner site and a Cl atom that was adsorbed to the upper terrace remains bound to the surface at an intermediate height. After the second copper atom is removed, the Cl atom binds to the lower terrace. The intermediate structure (-1 Cu) is energetically unfavorable, so removing the second copper atom is much more energetically favorable than removing the first copper atom. Figure S10 highlights this energetic effect. The removal of atoms b, g, j, k, n, and o is significantly more energetically

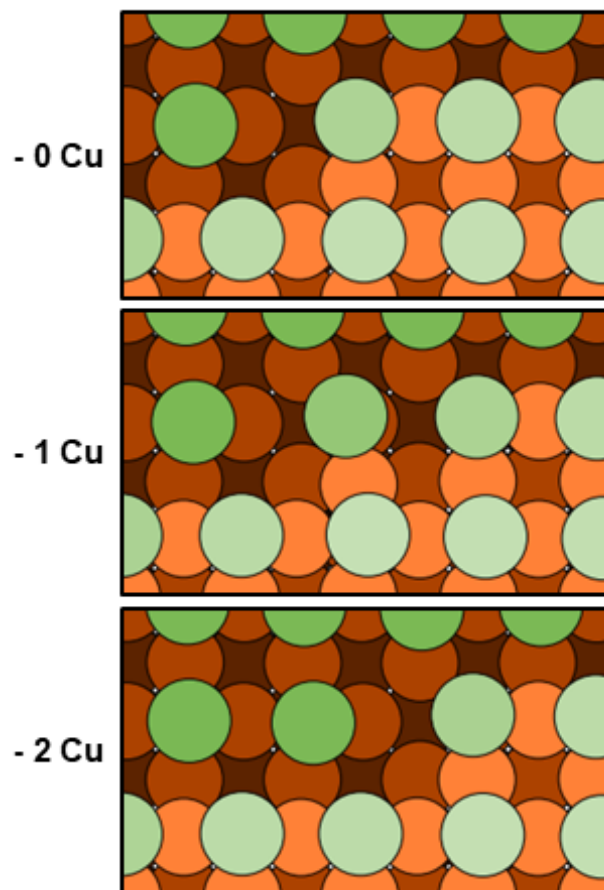


Figure S9: A schematic depicting our modeled Cu dissolution reaction from S_2 steps. Two Cu atoms are sequentially removed, and a Cl atom rebinds to the lower terrace to extend the Cl adlattice on the lower terrace.

favorable than the removal of the corner atoms shown in the main text.

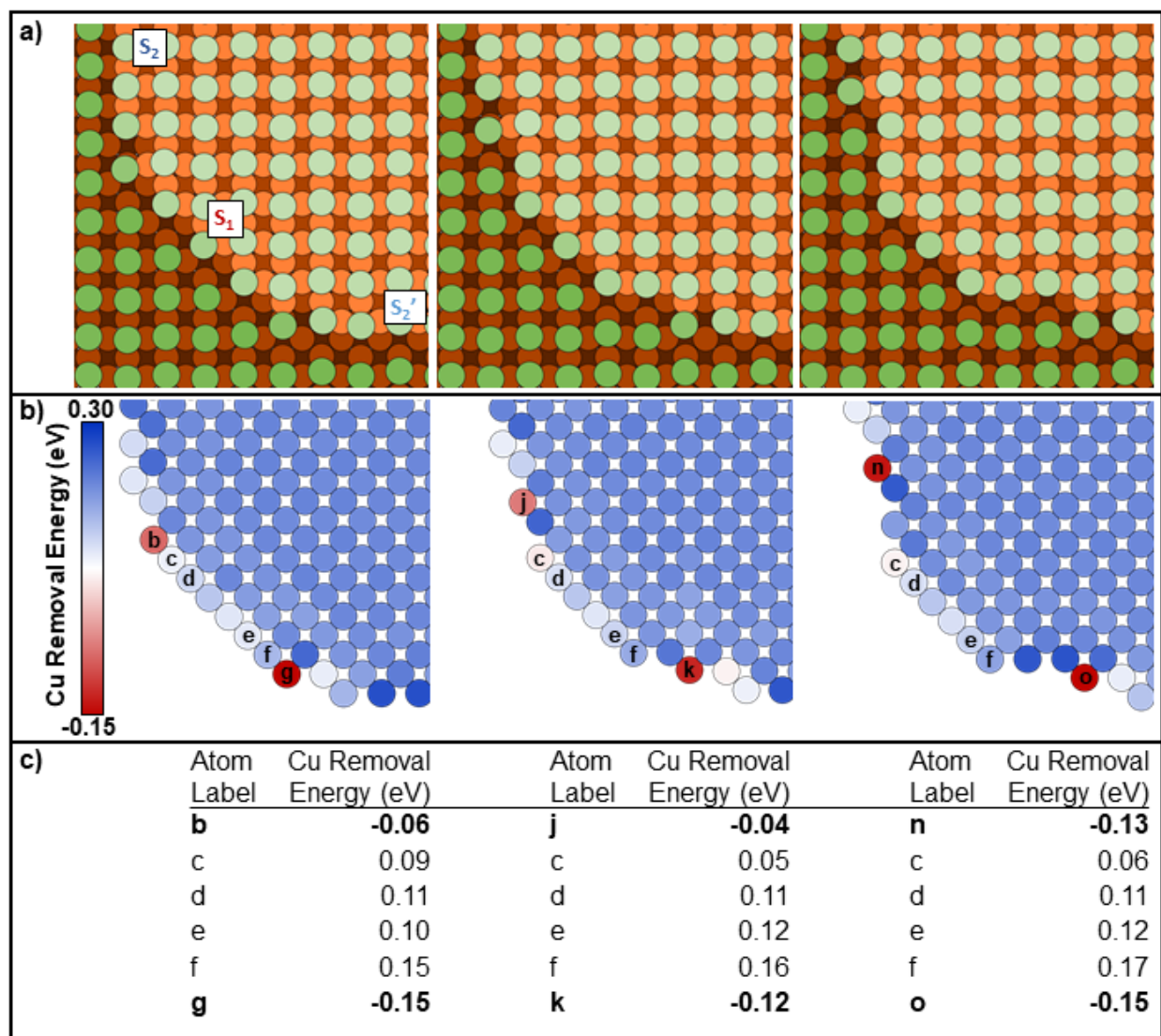


Figure S10: a) Schematic of copper dissolution occurring at the intersection of S₂-S₁, and S₁-S₂' steps on a copper monolayer step island covered in Cl. The left panel shows the pristine steps. The middle and right panels show the island with two Cu atoms removed from both the S₂ and S₂' steps (See SI for the intermediate steps). b) Heatmaps of the energy required to remove any individual Cu atom from the islands shown in (a) while leaving Cl adsorbed to the surface. Adsorbed Cl is not shown for clarity. c) removal energies for atoms labeled in (b).